



Fatigue crack propagation analysis in 2024-T351 aluminium alloy using nonlinear parameters

M.F. Borges^a, P. Lopez-Crespo^{b,*}, F.V. Antunes^a, B. Moreno^b, P. Prates^{a,c}, D. Camas^b, D. M. Neto^a

^a Univ Coimbra, Centre for Mechanical Engineering, Materials and Processes (CEMMPRE), Department of Mechanical Engineering, Portugal

^b Department of Civil and Materials Engineering, University of Malaga, C/ Doctor Ortiz Ramos, s/n, 29071, Malaga, Spain

^c Department of Mechanical Engineering, Center for Mechanical Technology and Automation (TEMA), University of Aveiro, 3810-193 Aveiro, Portugal

ARTICLE INFO

Keywords:

Fatigue crack growth (FCG)
Crack tip opening displacement (CTOD)
Cyclic plastic behaviour
Aluminium alloy

ABSTRACT

In this work, fatigue crack growth (FCG) in the 2024-T351 aluminium alloy is studied using the plastic CTOD range, $\Delta\delta_p$. Experimental tests were performed on 12 mm thick CT specimens in order to obtain FCG rate and in cylindrical specimens to obtain stress-strain loops. A numerical analysis replicated the experimental work in terms of material, geometry and loading conditions, but assuming pure plane strain state, in order to obtain $\Delta\delta_p$. The material parameters were fitted using the experimental stress-strain loops. The experimental work showed an increase of FCG rate with the increase of stress ratio from $R = 0.1$ to $R = 0.7$ mm, which indicated the existence of the crack closure phenomenon. However, the analysis of the position of the first node behind the crack tip showed that there is no crack closure under plane strain state, while a maximum value of 36% was found for plane stress state. Therefore, the surfaces influence FCG rate even in 12 mm thick specimens. A nearly linear relation was found between da/dN and $\Delta\delta_p$. The comparison with other aluminium alloys showed that there is a significant influence of material on da/dN - $\Delta\delta_p$ relation. The change from plane strain to plane stress state decreased FCG rate due to crack closure. Under plane strain state there is a minor influence of stress ratio in the range $R = 0.1$ - 0.7 , also because there is no crack closure. Finally, a comparison was made between plastic CTOD and cumulative plastic strain at the crack tip. Well defined relations were found, showing that both parameters can be used to quantify crack tip deformation.

1. Introduction

Fatigue crack propagation is usually studied assuming that the range of stress intensity factor, ΔK , is the driving force [1]. In fact, there is a link between the singular elastic field and the plastic deformation happening at the crack tip [2], which justify the extensive use of ΔK . The da/dN - ΔK curves of each material are obtained experimentally in standard specimens [3]. Different limitations have however been identified in the use of these da/dN - ΔK curves, namely, the increase of da/dN with stress ratio, the incapacity to explain load history effects and the relatively high fatigue crack growth (FCG) rate observed for short cracks. Besides, the use of ΔK is limited to Linear Elastic Fracture Mechanics, whose definition of limits is not obvious [4]. Therefore, different concepts have been proposed to circumvent these limitations and at the head of them appear the concept of crack closure [5]. The contact of crack flanks has been widely used to explain the effect of stress ratio,

specimen thickness, variable amplitude loading and short cracks. However, despite its ability to explain different FGC issues, crack closure has been the subject of heated discussions. In fact, there is no consensus about the adequate measurement procedure, and there are researchers questioning its relevance on FCG [6]. Complementary concepts, like the T-stress [7,8] and more complex models, like the Christopher-James-Patterson (CJP) model [9], were also proposed. An alternative approach based on K_{max} and ΔK was proposed [10,11], which shifts attention from behind the crack tip to its front.

However, for a better understanding of FCG, attention must be focused on the crack tip. In fact, since FCG is due to irreversible damage acting at the crack tip, alternative parameters to the elastic ΔK are needed. Different damage mechanisms may be active at the crack tip, but cyclic plastic deformation is usually considered to be the most relevant [12,13]. Consequently, different nonlinear parameters have been proposed as crack driving forces, including the total CTOD (Crack

* Corresponding author.

E-mail address: plopezcrespo@uma.es (P. Lopez-Crespo).

<https://doi.org/10.1016/j.ijfatigue.2021.106478>

Received 9 April 2021; Received in revised form 5 August 2021; Accepted 8 August 2021

Available online 12 August 2021

0142-1123/© 2021 The Authors.

Published by Elsevier Ltd.

This is an open access article under the CC BY-NC-ND license

(<http://creativecommons.org/licenses/by-nc-nd/4.0/>).

Tip Opening Displacement), the energy dissipated around the crack tip, the plastic deformation at the crack tip [14,15], and the size of the cyclic plastic zone [16,17]. The authors proposed the correlation of da/dN with the plastic CTOD range, $\Delta\delta_p$, and obtained linear $da/dN-\Delta\delta_p$ plots in natural scales [18,19]. Two assumptions are behind the use of plastic CTOD as crack driving force: (1) FCG is due to cyclic plastic deformation. (2) The plastic CTOD is able to feel crack tip phenomena, being proportional to crack tip deformation. The determination of $da/dN-\Delta\delta_p$ curves follows a simple strategy. First, experimental work using standard specimens (C(T) or M(T)) is followed in order to obtain da/dN . Second, a finite element model replicates the experimental work in order to predict the plastic CTOD. The numerical model must replicate the experimental work in terms of loads, geometry and material properties. The proper modelling of material behaviour is fundamental to obtain good quality predictions of plastic CTOD. The material constants, including the isotropic and kinematic hardening parameters, are obtained in low-cycle fatigue tests, using cylindrical specimens tested under constant strain range. The difference between the experimental stress-strain loops and analytical models are minimised in order to obtain material constants. The CTOD has also been determined experimentally using Digital Image Correlation (DIC) [20–23]. More recently, a predictive model based on cumulative plastic strain at the crack tip was developed [25,26]. This needs only one experimental value of da/dN , while the $da/dN-\Delta\delta_p$ approach needed values for several crack lengths. However, DIC cannot be used to calculate the crack tip plastic deformation.

The main objective here is to study FCG in the 2024-T351 aluminium alloy using nonlinear crack tip parameters. Experimental work was developed in CT specimens to obtain FCG rate and in cylindrical specimens to obtain stress-strain loops. A numerical model was developed to predict plastic CTOD, $\Delta\delta_p$, in order to obtain a $da/dN-\Delta\delta_p$ model. This model was compared with similar ones obtained previously for other aluminium alloys and was used to predict the effect of stress state and stress ratio. In addition, an attempt was made to verify the existence of a link between the plastic CTOD range and the crack tip plastic strain. This is important to ensure that DIC can continue to be used in the new approach based on crack tip plastic strain.

2. Experimental fatigue crack growth rate

Table 1 shows the chemical composition of the 2024-T351 aluminium alloy used in this work. Table 2 presents the mechanical properties of the 2024-T351 aluminium alloy. Young modulus, Yield stress, and Ultimate Tensile Strength (UTS) and elongation at break were determined with a tensile test. This material has a low environmental impact, good fatigue properties, and high specific properties. Therefore it is interesting for transportation industries [27]. This means that these types of alloys are ranked favourably when both fatigue behaviour and environmental impact are taken into account. In fact, this material is the most used aluminium alloy in the aircraft industry. With respect to corrosion resistance, it should also be noted that Al-Cu alloys are rather sensitive to aqueous NaCl solutions.

FCG experiments were conducted on C(T) specimens with $W = 50$ mm and thickness of 12 mm, following ASTM E-647 standard [3]. The specimens were machined in T-L direction. Therefore crack growth occurs along the rolling direction. The tests were performed in a 100kN servo-hydraulic testing machine. The specimen was pre-cracked under mode I loading for 120,000 cycles at a frequency of 10 Hz, a load ratio (R) of 0.05 and a stress intensity range (ΔK) of 8 MPa-m^{0.5}. The

Table 1

Chemical composition in weight % of 2024-T351 aluminium alloy. The balance is Al [28].

Si	Fe	Cu	Mn	Mg	Cr	Zn	Ti
0.50	0.50	3.8–4.9	0.3–0.9	1.2–1.8	0.10	0.25	0.15

Table 2

Mechanical properties of 2024-T351 aluminium alloy [28].

Young modulus	Yield Stress	UTS	Elongation at Break	Brinell Hardness
73 GPa	325 MPa	470 MPa	20%	137

final crack length of pre-cracking was about 20 mm ($a/W = 0.40$). All subsequent load cycles were done under constant amplitude loading, considering the loads presented in Table 3. The crack growth rates, da/dN , were obtained by numerical derivation in accordance with ASTM E647. The procedure involves fitting a parabola of order 5 to a set of 11 successive points in the $a-N$ curve and calculating the growth rate from the derivative of the parabola. Successive points in the $a-N$ curve were taken at 1500-cycle intervals.

Fig. 1 presents the fatigue crack growth rate, da/dN , versus ΔK in log-log scales for stress ratios $R = 0.1$ and $R = 0.7$ [29,30]. The increase of ΔK increases over da/dN , as expected, and regimes I and II of crack growth can be identified. A wavy behaviour can be seen in Paris law regime [29]. The fatigue thresholds for $R = 0.1$ and $R = 0.7$ are 3.3 and 1.79 MPa-m^{0.5}, respectively. The increase of stress ratio increases fatigue crack growth rate, which suggests the existence of crack closure for $R = 0.1$ [29].

3. Material hardening model

3.1. Strain controlled tests in smooth specimen

Cylindrical specimens were machined with 8 mm in diameter and a gauge section of 33.6 mm, in accordance with ASTM E606 standard [31]. The low cycle fatigue tests were conducted in a 100kN servo-hydraulic testing machine in laboratory air environment at room temperature. Tests were conducted under axial total strain-controlled mode, with sinusoidal waves, using a constant nominal strain rate of 0.008 s⁻¹, total strain ratio (R_ϵ) of -1 and total strain amplitude ($\Delta\epsilon/2$) equal to 0.02%. The strain was measured with a 12.5 mm gauge extensometer attached to the specimen using rubber bands. Fig. 2 shows the stress-strain curve obtained. The material presents initial cyclic hardening, followed by stabilisation.

3.2. Calibration of material parameters

The accurate modelling of material elastic-plastic behaviour is fundamental to obtain good quality numerical predictions of plastic CTOD. The elastic behaviour is assumed isotropic and described by Hooke's law. On the other hand, the plastic behaviour is characterised by the von Mises yield criterion and the Swift isotropic hardening law coupled with Lemaître-Chaboche kinematic hardening law under an associated flow rule. Swift hardening law is described by [32]:

$$Y = C \left[\left(\frac{Y_0}{C} \right)^{\frac{1}{n}} + \bar{\epsilon}^p \right]^n \quad (1)$$

where Y_0 , C , $\bar{\epsilon}^p$ and n are the material parameters. The Lemaître-Chaboche kinematic hardening law is [33]:

Table 3

Load parameters adopted in the experimental and numerical analysis.

R	F_{min} [N]	F_{max} [N]	a_{min} [mm]	a_{max} [mm]	$F_{min, num}$ [N]	$F_{max, num}$ [N]
0.1	500	5000	12	30	4.17	41.67
0.3	1680	5600	12	29	14.00	46.67
0.5	4250	8500	12	26.7	35.42	70.83
0.7	8750	12,500	12	22.5	72.92	104.17

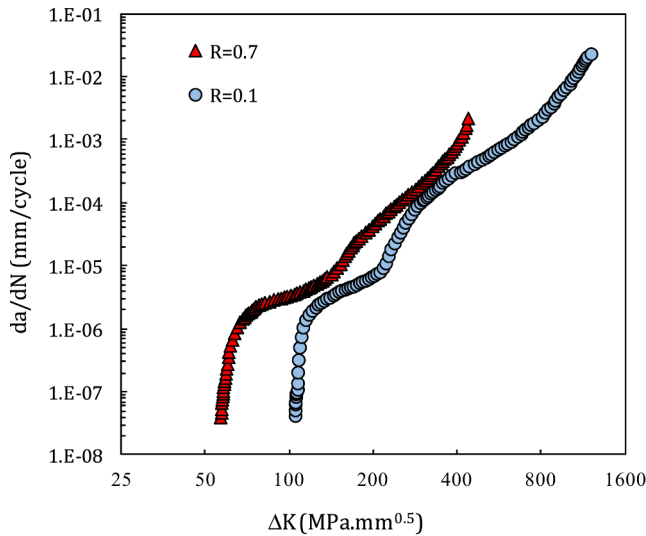


Fig. 1. Influence of the stress ratio on the da/dN - ΔK curves obtained experimentally for AA2024-T351.

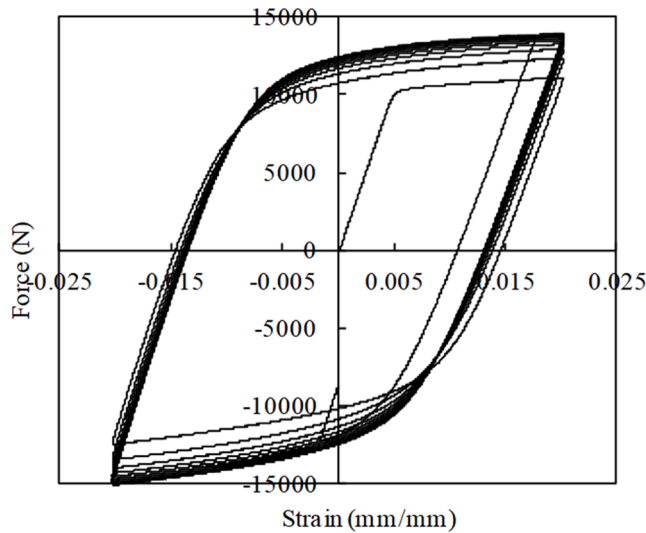


Fig. 2. Cyclic behaviour of the material.

$$\dot{X} = C_X \left[X_{Sat} \frac{\bar{\sigma}' - X}{\bar{\sigma}} - X \right] \dot{\varepsilon}^p, \quad (2)$$

where C_X and X_{Sat} are the material parameters of Lemaître-Chaboche law, $\bar{\sigma}$ is the equivalent stress and $\dot{\varepsilon}^p$ is the equivalent plastic strain rate. The calibration of the material parameters that best describe the plastic behaviour was made out by minimising the following least-squares objective function:

$$F(\mathbf{A}) = \sum_{i=1}^N \left(\frac{\sigma^{Fit}(A) - \sigma^{Exp}}{\sigma^{Exp}} \right)_i^2, \quad (3)$$

where $\sigma^{Fit}(A)$ and σ^{Exp} denote the fitted and the experimental values of true stress, respectively. The adopted experimental values were obtained from the low-cycle fatigue test carried out for $R_\varepsilon = -1$ and $\Delta\varepsilon/2 = 1.5\%$, using N experimental points. The set of material parameters (Swift and Lemaître-Chaboche laws) is defined by \mathbf{A} , which minimises $F(\mathbf{A})$. The fitting was carried out using the Microsoft Excel SOLVER, which uses the Generalised Reduced Gradient (GRG2) nonlinear optimisation algorithm [34]. The obtained set of material parameters is presented in

Table 4

List of material parameters involved in the Swift and Lemaître-Chaboche laws.

Material	Y_0 [MPa]	C [MPa]	n	C_x [-]	X_{Sat} [MPa]
2024-T351	288.96	389.00	0.056	138.80	111.84

Table 4. Fig. 3 shows the experimental and fitted stress plastic strain curves of the AA2024-T351. It is observed a superposition of the curves meaning that the set of parameters presented in Table 4 describe well the elastic-plastic behaviour of the material.

4. Numerical prediction of plastic CTOD

4.1. Finite element model

The C(T) specimen was modelled numerically using the finite element method. Only half of the specimen was modelled using suitable boundary conditions, as illustrated in Fig. 4a. A small thickness ($t = 0.1$ mm) was considered in the numerical models, which is enough to simulate plane stress and plane strain states considering adequate boundary conditions. Pure plane strain state was assumed, imposing restrictions to deformation perpendicularly to the main face, as shown in Fig. 4e. This stress state was assumed because the C(T) specimen used in the experimental tests is relatively thick (12 mm). A pure plane stress state was also simulated, eliminating the restrictions perpendicular to the main face of the specimen, as shown in Fig. 4d.

A straight crack was defined, with different initial sizes, a_0 , of 5, 9, 11.5, 14, 16.5, 19, 21.5, 24, and 26.5 mm. The constants presented in Table 4 were used to simulate the elastic-plastic behaviour of the material, while the loads in Table 3 were applied as indicated in Fig. 4a. The finite element model had a total number of 3D 7287 linear isoparametric elements and 14,918 nodes. The finite element mesh, shown in Fig. 4b and 4c, was refined in the crack growth region, having $8 \times 8 \mu\text{m}^2$ of the element size. The region with refined meshed was shifted in accordance with the initial crack length. Only one layer of elements was considered along the thickness direction. In the present study, crack propagation was numerically modelled by successive debonding of both current crack front nodes. The release occurs at minimum load to avoid convergence problems that could arise by propagating the crack at maximum load. The size of each crack increment corresponded to the finite element size in the refined region, and five load cycles were applied between successive increments. In order to stabilise the plastic wake, 800 load cycles were applied, corresponding to a total crack propagation $\Delta a = 1.272$ mm.

The numerical simulations were performed using the three-dimensional elastic-plastic finite element code DD3IMP [35,36]. An updated Lagrangian approach is used to describe the evolution of the

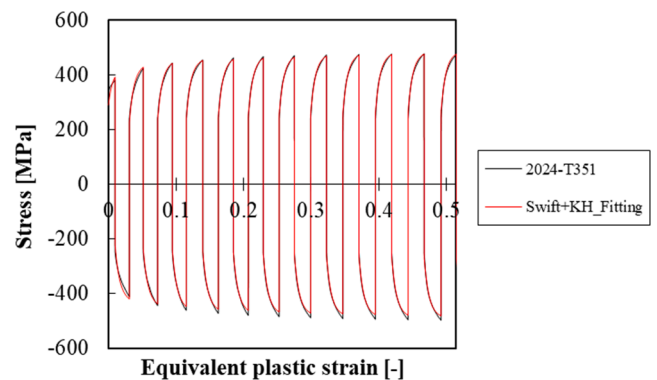


Fig. 3. Cyclic stress - plastic strain curve of AA2024-T351 (black line) and fitted curve (red line), obtained by minimisation of $F(\mathbf{A})$. (For interpretation of the references to colour in this figure legend, the reader is referred to the web version of this article.)

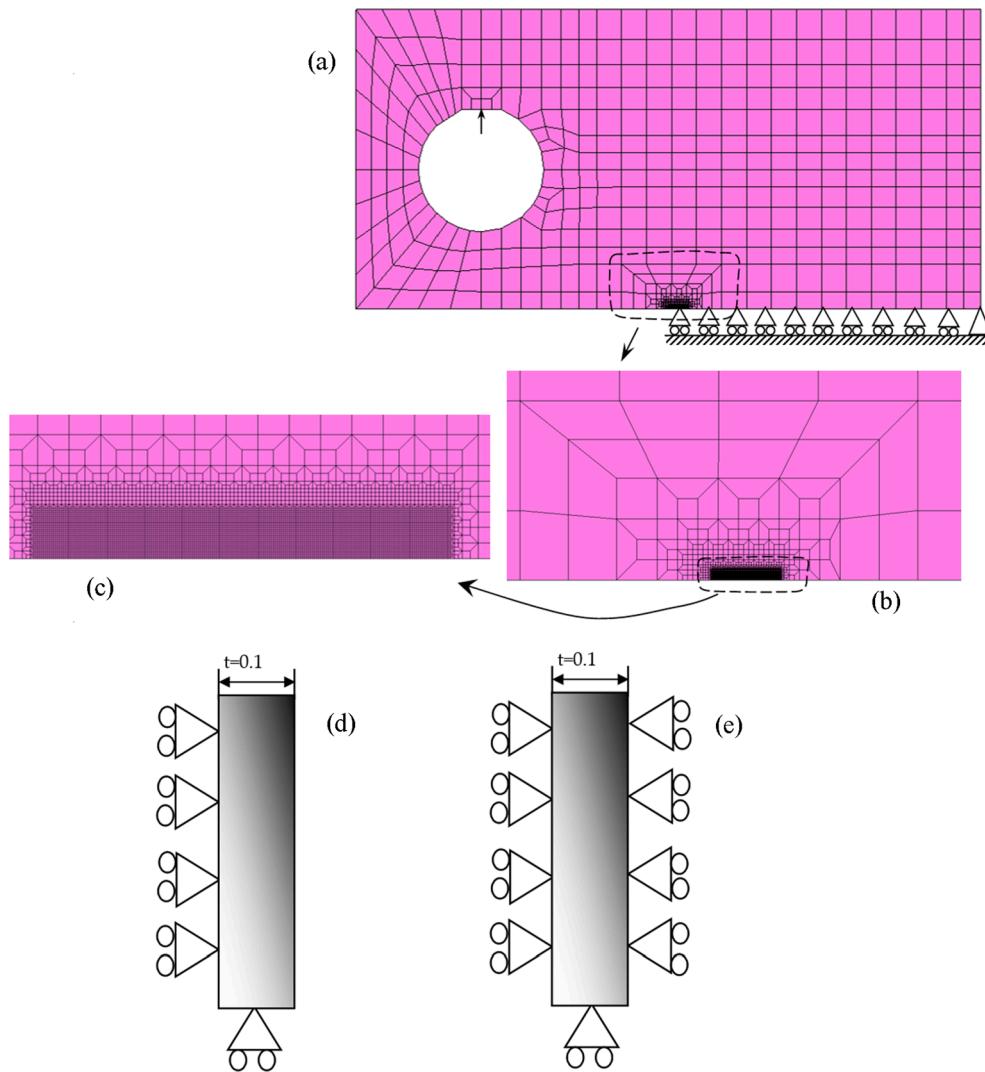


Fig. 4. Model of C(T) specimen. (a), (d) and (e) Load and boundary conditions. (b) and (c) Details of finite element mesh.

deformation process, assuming a hypoelastic–plastic model. The numerical model considers large elastoplastic strains and rotations, while the elastic strains are assumed negligibly small. In order to take into account the physical contact between the crack flanks, a rigid body (plane surface) aligned with the crack symmetry plane is considered. The CTOD was measured at the first node behind the crack tip, i.e., at a distance of 8 μm from the crack tip.

4.2. Numerical results

4.2.1. Typical plots of CTOD versus F

Fig. 5 presents typical results of CTOD versus the ratio between the nominal stress at the crack tip and the yield stress of the material, obtained after a crack growth $\Delta a = 1.272$ mm, corresponding to 159 increments of 8 μm . In this case, the crack is open at the minimum load (point A), which means that there is no crack closure. This can be considered normal for plane strain state. The progressive loading increases the CTOD, and up to point B there is a linear elastic behaviour. The load range between A and B is used to predict the elastic range of ΔK and the fatigue threshold. Plastic deformation starts at point B, increasing progressively up to the maximum load (point C). The range of plastic CTOD, δ_p , is represented by $\Delta\delta_p$. The subsequent decrease of load produces reversed elastic and plastic deformation. The reversed plastic deformation, $\Delta\delta_{pr}$, is lower than $\Delta\delta_p$.

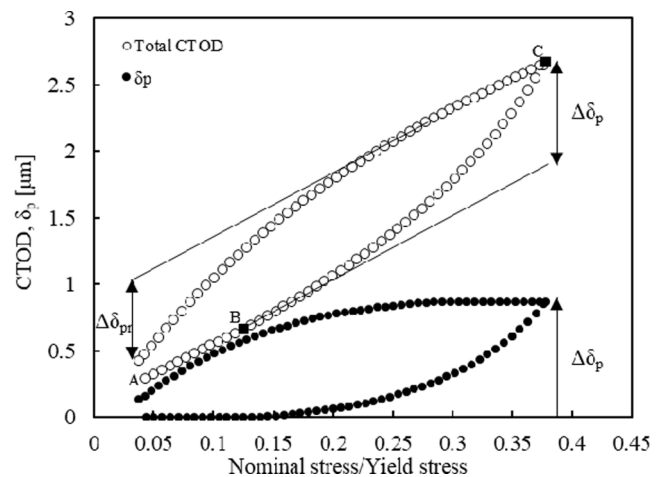


Fig. 5. Typical results of CTOD versus the ratio between the nominal stress evaluated at the crack tip and the yield stress of the material ($a = 22.772$ mm; $F_{\text{max}} = 41.67$ N; $F_{\text{min}} = 4.16$ N; $R = 0.1$; $\Delta K = 14.20$ $\text{MPa}\cdot\text{m}^{0.5}$; plane strain).

4.2.2. Prediction of fatigue threshold

The CTOD results may also be used to predict the effective ΔK , obtained removing the elastic range of load. The load range between points A and B in Fig. 5 defines the elastic range, which is not expected to contribute to FCG. Fig. 6 plots ΔK_{elas} versus plastic CTOD range, $\Delta\delta_p$, obtained for the different crack lengths studied. The decrease of $\Delta\delta_p$ (i.e., of ΔK) produces a negligible linear decrease of ΔK_{elas} from about $3.88 \text{ MPa}\cdot\text{m}^{0.5}$ to $3.67 \text{ MPa}\cdot\text{m}^{0.5}$. There is no influence of stress ratio, which is a good indication for the robustness of the predictions. Note that crack closure is removed from the analysis, which explains the independence relatively to stress ratio, R . On the other hand, the experimental values show a significant influence of the stress ratio due to crack closure [37]. Note that the effective range of ΔK is expected to be $K_{max} - K_{open} - \Delta K_{elas}$ ($=K_{max} - K_B$, being K_B the stress intensity factor corresponding to the transition between the elastic and plastic regimes). The extrapolation of ΔK_{elas} to zero gives the effective fatigue threshold, $\Delta K_{th,eff}$, assuming that the fatigue threshold corresponds to a pure elastic deformation at the crack tip. The value obtained for $\Delta K_{th,eff}$ was about $3.46 \text{ MPa}\cdot\text{m}^{0.5}$, as can be seen in Fig. 6.

Experimental results for $R = 0.1$ and $R = 0.7$ are also presented in Fig. 6, which were obtained from Fig. 1. Crack closure for $R = 0.7$ is null or almost negligible, therefore, the fatigue threshold can be considered to be an effective value. On the other hand, the value for $R = 0.1$ is higher due to crack closure. The numerical prediction of $\Delta K_{th,eff}$ is significantly higher than the experimental value, by a factor of about 2. This is just an empirical rule, but it seems to work, i.e., there is a factor of about 2 between the numerical prediction of fatigue threshold and the effective value obtained experimentally [38]. The difference may be explained by environmental mechanisms which are dominant for nearly stationary fatigue crack [39]. In fact, the 2024 alloy is affected by oxidation and hydrogen embrittlement [40]. Therefore, the numerical approach proposed for the prediction of fatigue threshold is adequate for vacuum conditions [38]. Avram [41] obtained $\Delta K_{th} = 3.8 \text{ MPa}\cdot\text{m}^{0.5}$ for 2024-T351 aluminium alloy tested at $R = 0.1$ (M(T) specimens; $W = 101.6 \text{ mm}$; $t = 9.5 \text{ mm}$), which is quite similar to the value obtained here in CT specimens. Broek and Schijve [42] tested the 2024-T3 aluminium alloy and obtained fatigue threshold values of 3.2, 2.9 and $1.2 \text{ MPa}\cdot\text{m}^{0.5}$ for $R = 0.06, 0.3$ and 0.64 , respectively.

4.2.3. Evaluation of crack closure

The crack closure phenomenon usually has a significant impact on FCG. Therefore it must be quantified for a better understanding of the results. The results in Fig. 1, namely the variation of da/dN with the change of stress ratio from 0.1 to 0.7, indicate the existence of crack closure for $R = 0.1$. Fig. 7 presents the variation of crack closure with ΔK ,

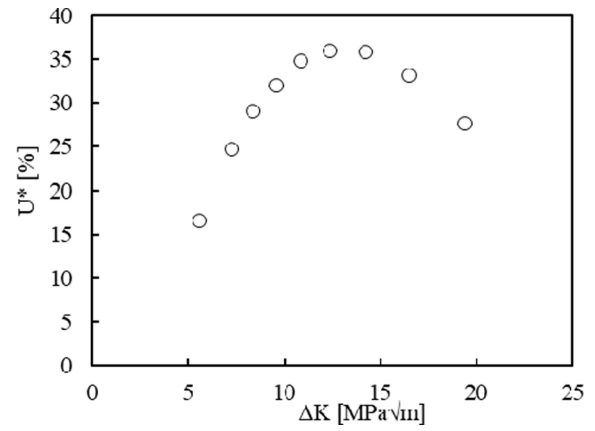


Fig. 7. Crack closure versus ΔK ($F_{min} = 4.17 \text{ N}$; $F_{max} = 41.67 \text{ N}$; $R = 0.1$; plane stress state).

obtained from the CTOD plots, i.e., from the analysis of contact status of the first node behind the crack tip, for plane stress state. The crack opening level was quantified by:

$$U^* = \frac{F_{open} - F_{min}}{F_{max} - F_{min}} \times 100, \quad (4)$$

where F_{open} is the crack opening load. This parameter quantifies the percentage of load range during which the crack is closed. No crack closure was observed for plane strain state, even for $R = 0.1$, as illustrated in Fig. 5. The change to plane stress state produces a significant increase of crack closure phenomenon, as could be expected. The stress triaxiality associated with the plane strain state reduces the plastic deformation level at the crack tip, and therefore crack closure. In plane stress state, it is observed a parabolic development of U^* with ΔK , as can be seen in Fig. 7, being the concavity of the curve facing down, i.e., there is an increase of U^* for lower crack lengths, up to a peak, where U^* reaches 36%. For higher crack lengths, U^* decreases. The increase of ΔK produces an increase of reversed plastic deformation, and therefore a decrease of crack opening level. The increase of K_{max} increases monotonic plastic deformation and consequently of crack opening level.

On the other hand, the increase of K_{max} increases crack tip blunting, decreasing U^* . The effect of crack tip blunting is commonly observed at tensile overload events, in which crack closure is drastically reduced and, in many tests, eliminated. Therefore, up to $U^* = 36\%$, the increase of monotonic plastic deformation is dominant, while above 36% crack tip blunting and reversed plastic deformation are more relevant.

The observation of crack closure effect on the experimental results (Fig. 1) indicates that, although the relatively high thickness of the specimen, the plane stress state observed near corner points has a significant effect on FCG rate.

4.2.4. Multi-point modeling of fatigue crack growth

The plastic CTOD range, $\Delta\delta_p$, indicated in Fig. 5 quantifies the crack tip plastic deformation. Therefore, it is expected to be the driving force for FCG. Fig. 8a plots the experimental FCG rate (da/dN) versus the predicted $\Delta\delta_p$, obtained for the same conditions. The increase of $\Delta\delta_p$ is accomplished by the increase of da/dN , as could be expected since more crack tip plastic deformation produces a faster crack growth. A second-order polynomial was fitted by regression, which is represented by the filled line. The corresponding analytical expression is:

$$\frac{da}{dN} = 0.0892\Delta\delta_p^2 + 0.3707\Delta\delta_p, \quad (5)$$

where the units of da/dN and $\Delta\delta_p$ are $\mu\text{m}/\text{cycle}$ and μm , respectively. This is supposed to be a material property, which can be used to predict the effect of load parameters and geometry. Note that the $da/dN - \Delta K$

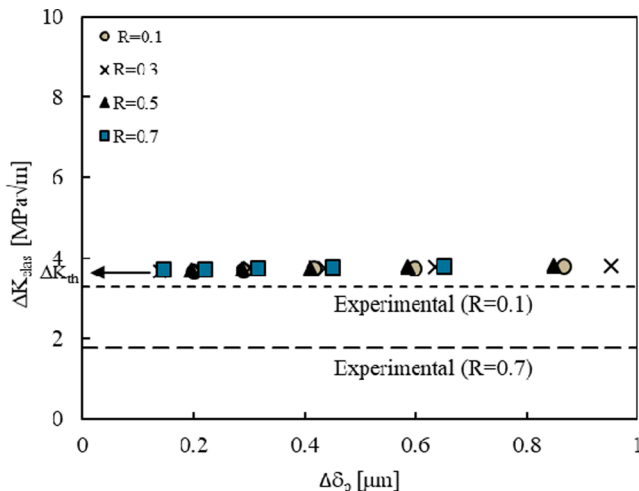


Fig. 6. ΔK_{elas} versus plastic CTOD range, $\Delta\delta_p$ (plane strain state).

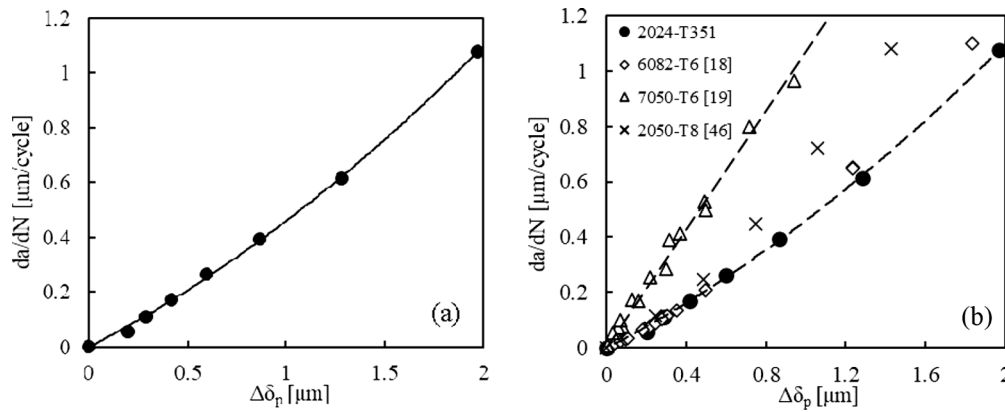


Fig. 8. da/dN versus $\Delta\delta_p$ model (a) Results for the 2024-T351 aluminium alloy ($R = 0.1$; plane strain). (b) Comparison with other aluminium alloys.

approach is not a material property and cannot be used for predictions. A linear relation could be expected between da/dN and $\Delta\delta_p$, as was observed experimentally [22,24], but the slight deviation observed in Fig. 8a may be explained by a change of stress state not modelled numerically. In fact, as the crack grows, there is a trend for the plane stress state, while the numerical model always assumes a pure plane strain state. This modelling problem can only be solved with 3D realistic models, which are addressed for future work.

The literature presents other models relating da/dN with nonlinear crack tip parameters. Pommier and Risbet [43] proposed that da/dN depends on total CTOD: $da/dN \approx \alpha/2 \cdot \Delta\text{CTOD}/2$. The α parameter is to be adjusted from fractographic experiments [44] or by fitting the model to da/dN results. Seifi and Hosseini [45] presented $da/dN-\Delta J$ plots for raw and annealed copper. da/dN was obtained experimentally while ΔJ was predicted numerically. Linear relations were obtained in log-log scales.

Fig. 8b compares the behaviour of the 2024-T351 alloy with results for other materials obtained in previous works [18,19,46]. The dashed lines were added to define the upper and lower bound for all the results. There is a significant influence of material on $da/dN-\Delta\delta_p$ model, which means that for the same crack tip plastic deformation, the FCG rate produced greatly depends on microstructure. Vasco-Olmo et al. [24] studied the 2024-T3 and 7050-T6 aluminium alloys and also obtained distinct $da/dN-\Delta\delta_p$ models. In their study, $\Delta\delta_p$ was extracted from CTOD plots obtained experimentally using Digital Image Correlation (DIC). Regardless, some influence of errors of experimental values of da/dN and of the numerical predictions of $\Delta\delta_p$ may exist. Several numerical parameters may affect the numerical predictions, namely the number of load cycles between crack increments and the finite element mesh.

4.2.5. Prediction of FCG rate for different stress states and stress ratios

Fig. 9a shows predictions of da/dN , for plane strain and plane stress

states, in log-log scales. A plane stress model was used to predict the plastic CTOD range, $\Delta\delta_p$, which was inserted in Eq. (5) to obtain da/dN . A comparison was made with plane strain results and experimental results. A good agreement exists between the plane strain predictions and the experimental results because Eq. (5) was obtained for plane strain conditions. The plane stress state gives lower values of da/dN mainly because of crack closure phenomenon. As previously said, no crack closure was found for the stress ratios when considering plane strain state. However, as can be seen in Fig. 7, the plane stress state is deeply affected by the crack closure, which diminishes the effective load range.

Fig. 9b predicts the effect of stress ratio on da/dN for plane strain state, in logarithmic scales. As can be seen, for higher ΔK the data is overlapped, meaning that there is no visible influence of stress ratio on da/dN , due to the absence of crack closure. There is a small difference in values for relatively low ΔK . Indeed, in this region, it is observed, for the same ΔK , an increase of da/dN with R . This increase of da/dN with R is a well-known experimental trend. Seifi and Hosseini [45] in pure copper ($R = 0.077; 0.2$) also observed that the increase of stress ratio increases da/dN .

4.2.6. Prediction of the effect of stress ratio, maintaining ΔK constant

Another study was made to predict the effect of stress ratio on da/dN and crack closure, maintaining ΔK constant. Accordingly, a specific value of a_0 was defined ($a_0 = 21.5 \text{ mm}$), and the loading parameters were adjusted, leading to a constant ΔK equal to $15.15 \text{ MPa}\cdot\text{m}^{0.5}$. Table 5 presents the different stress ratios and load parameters defined in this study. As previously, all fatigue cracks propagated at minimum load, at every 5 load cycles, with total crack propagation equal to 1.272 mm.

Fig. 10a shows da/dN versus R , for plane strain and plane stress states. The prediction of da/dN was made with equation (5). There is an increase of da/dN with stress ratio for both plane strain and plane stress

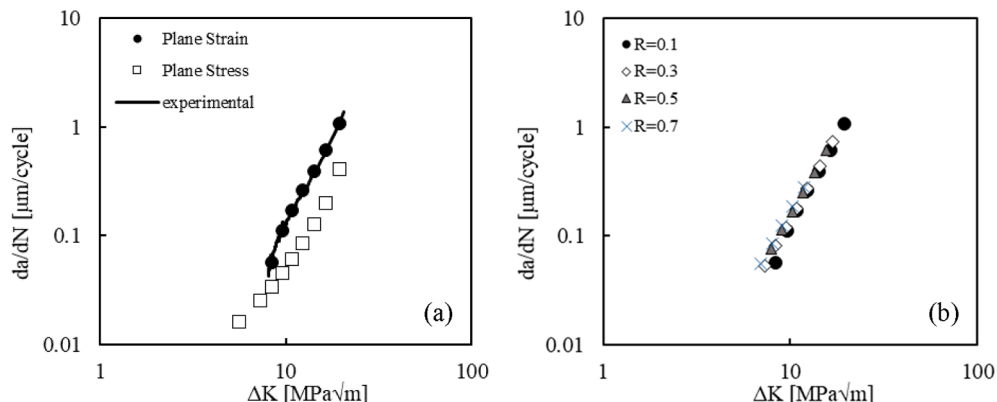


Fig. 9. Prediction of the effect of: (a) Stress state ($R = 0.1$). (b) Stress ratio (plane strain).

Table 5
Stress ratios and load parameters.

R	F_{min} [N]	F_{max} [N]
-1	-20	20
-0.6	-15	25
-0.33	-10	30
0	0	40
0.20	10	50
0.43	30	70
0.55	50	90
0.63	70	110
0.71	100	140

states. The transition of minimum load from compression to tension has a significant influence of FCG rate. In plane strain state a significant difference exists between negative and non-negative stress ratios. For positive stress ratios, there is a linear increase of da/dN with the stress ratio. This seems to contradict the results in Fig. 9b, where there is no evidence of the stress ratio effect in the range 0.1–0.7. However, it is noteworthy that da/dN is plotted in logarithmic scale in Fig. 9b and in natural scale in Fig. 10a. In fact, for positive stress ratios, da/dN only ranges from 0.45 to 0.63 μm . Besides, the load conditions are different. In Fig. 10a, a well-defined trend is observed for plane stress state. Anyway, for negative stress ratios, there is a slow increase of da/dN , while after $R = 0$ the rate of increase of da/dN raises. The FCG rate is lower in plane stress state for all stress ratios studied.

Fig. 10b plots U^* versus R . As expected, U^* decreases with R in both stress states, being U^* in the range [0–50%] in plane strain, and in the range [4–65%] in plane stress. There is a sudden decrease of U^* from $R = -0.6$ to $R = -0.33$, in plane strain state. However, the sudden increase of da/dN was observed from $R = -0.33$ to $R = 0$. For tensile stress ratios, no crack closure was found in plane strain state, being in accordance with section 4.2.3. For plane stress state, the rate of decrease of U^* is higher in tensile loading. Even for $R = 0.71$, which is a high stress ratio, there is some crack closure. This is relevant because it indicates that the usual assumption that there is no crack closure at relatively high stress ratios may be erroneous and may lead to incorrect conclusions.

5. Linking plastic CTOD and the accumulated plastic strain

In addition to CTOD, different parameters have been proposed to quantify plastic deformation at the crack tip, namely, the dissipated energy, the size of the reverse plastic zone, the ratcheting strain and plastic deformation ahead of the crack tip. In this section, the link between the plastic CTOD range, $\Delta\delta_p$, and the accumulated plastic strain, $\Delta\epsilon_p$ is established. This is relevant since the CTOD may be obtained experimentally through different full-field techniques [47]. Surface displacement information can be acquired via DIC [48,49]. Bulk

information can also be obtained through X-ray tomography [50,51]. The strain developed at the crack tip can also be measured by means of synchrotron X-ray diffraction [52]. Nevertheless, it is not possible to achieve a great through thickness resolution for strain measurement [53,54]. However, access to such synchrotron facilities is very limited. From an engineering design point of view, obtaining the crack tip strain measurement without the need to access synchrotron research centres would be greatly advantageous. Accordingly, this section aims at establishing the relationship between the plastic CTOD range, $\Delta\delta_p$, and the crack tip plastic strain. In this way, simple laboratory techniques such as DIC can be used in combination with the current numerical approach to estimate the crack tip strain.

The difficulty of the numerical measurement of the equivalent plastic strain at the crack tip [55,56], due to the singularity of the crack, was overcome by measuring the equivalent plastic strain at two Gauss points located around the crack tip (immediately behind and ahead), and then take the average. Fig. 11a and 11b show the development of the plastic CTOD, δ_p , and the equivalent plastic strain at the crack tip, ϵ_p , respectively, for a load cycle. There is a perfect match between the transition of regimes (elastic and elastic–plastic regime), i.e., at the elastic regimes (stretches A-B and C-D), ϵ_p remains constant, as expected, and so does δ_p . Thus, points A-E presented in Fig. 11a, and 11b occur at the same pseudo-time. The only difference occurs at the discharge of the specimen. Obviously, even during discharging, ϵ_p increases. In the case of δ_p , since CTOD generates a loop for every load cycle, there is a decrease during unloading.

Therefore, a very interesting link is observed between what is happening at the crack tip (ϵ_p) and behind the tip. This is very relevant because it indicates that different nonlinear crack tip parameters are different faces of the same coin and may be used to unify the approaches followed by different authors. Also, Fig. 11a and b show the extraction of $\Delta\delta_p$ and $\Delta\epsilon_p$, respectively. In this section, all values of $\Delta\delta_p$ and $\Delta\epsilon_p$ were calculated from plots corresponding to the last load cycle, at which occurs the last crack propagation. Of course, the extraction of these parameters can be made for any load cycle.

The procedure described above was performed for the simulations discussed in the previous sections. Fig. 12 shows the evolution of $\Delta\delta_p$ versus $\Delta\epsilon_p$ for the stress ratios $R = 0.1$ to 0.7, for different crack lengths and stress states. There is a well-defined relation between both nonlinear parameters, which indicates that both can be used to characterise crack tip plastic deformation. Quadratic polynomials were fitted, but the variation is almost linear, particularly for the lowest values of plastic deformation. The relation between $\Delta\delta_p$ and $\Delta\epsilon_p$ is independent of the stress ratio variable. However, there is some influence of stress state, which increases with plastic deformation level. This means that for the same value of $\Delta\epsilon_p$, two values of $\Delta\delta_p$ are obtained depending on the stress state.

Another study was made to link $\Delta\delta_p$ and $\Delta\epsilon_p$ when a single tensile

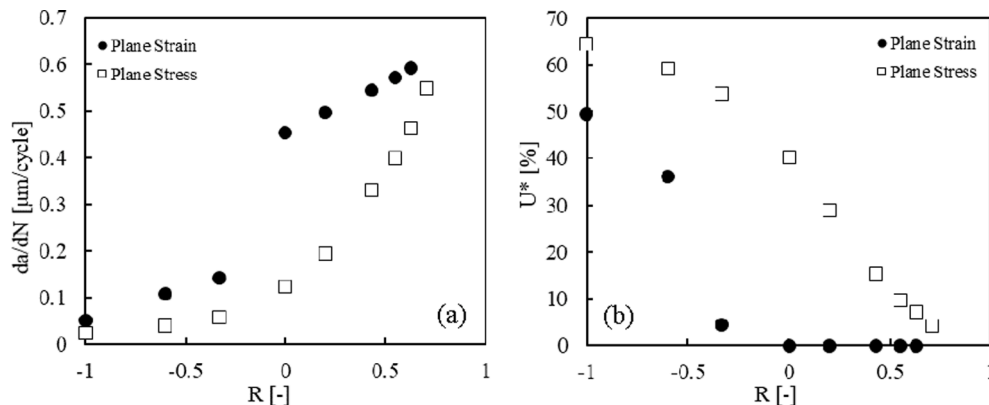


Fig. 10. Prediction of the effect of R on: (a) FCG rate. (b) Crack closure ($\Delta K = 15.15 \text{ MPa}\cdot\text{m}^{0.5}$).

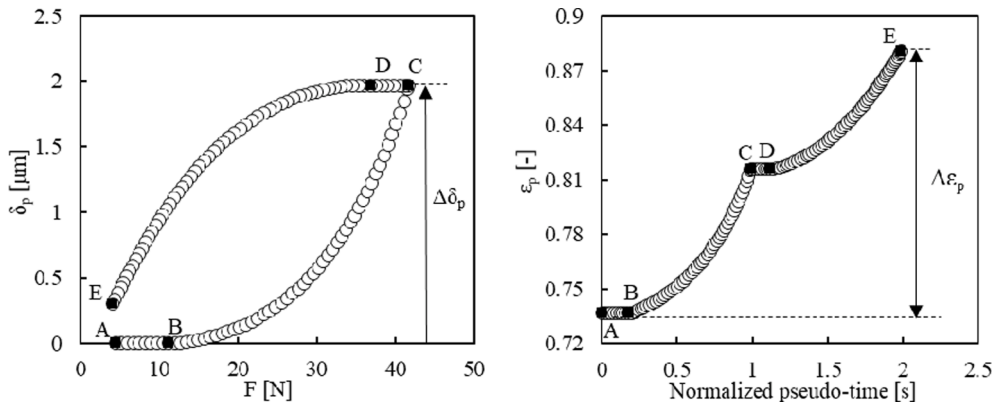


Fig. 11. Extraction of non-linear parameters: (a) $\Delta\delta_p$, (b) $\Delta\varepsilon_p$ ($R = 0.1$; $a = 27.772$ mm $\Delta K = 19.42$ MPa·m^{0.5}; plane strain).

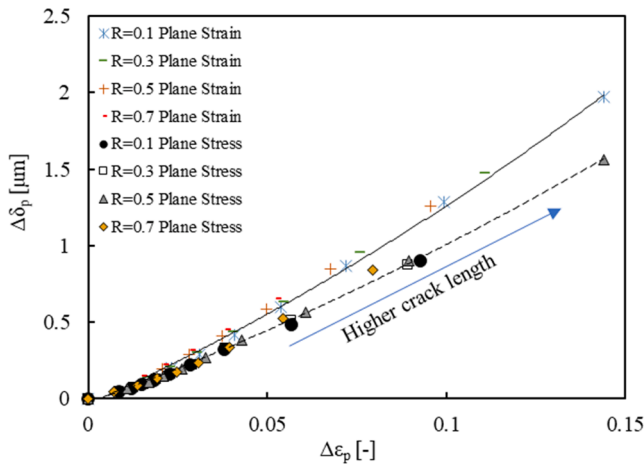


Fig. 12. Comparison of $\Delta\delta_p$ and $\Delta\varepsilon_p$ for different stress ratios, crack lengths and stress states.

overload (OL) is applied. This study was conducted in the same geometry as the previous sections (see Fig. 4). The load was applied at the top of the hole of the specimen, with baseline loads F_{max} and F_{min} equal to 41.67 N and 4.17 N, respectively, leading to $R = 0.1$, as presented in Table 3. The initial crack size, a_0 , was 16.5 mm. The crack size at which the overload was applied, a_{OL} , was 16.74 mm, with a peak load, F_{OL} , equal to 60.42 N, leading to an overload ratio, OLR, of 1.50. The overload ratio was defined as:

$$OLR = \frac{F_{OL} - F_{min}}{F_{max} - F_{min}}, \quad (6)$$

In contrast with the crack growth criterion previously studied, at which crack propagation occurred at every 5 load cycles, in this novel study, another crack growth criterion is adopted, based on the accumulated plastic strain, $\Delta\varepsilon_p$. This crack growth criterion called Total Plastic Strain (TPS) is based on the assumption that the damage accumulation controls FCG [26]. Accordingly, the crack propagation, i.e., the crack tip node release, occurs when $\Delta\varepsilon_p$ reaches a critical value [25]. The calibration of the critical value for the 2024-T351 was made in a previous work [25], where it was obtained $\Delta\varepsilon_p^c = 0.83$, comparing experimental da/dN and numerical predictions. As previously, to avoid convergence problems, the crack propagated at minimum load.

In Fig. 13 is plotted the development of $\Delta\delta_p$ versus $\Delta\varepsilon_p$ with the application of the tensile overload, in a plane stress state. Before the overload, $\Delta\delta_p$ and $\Delta\varepsilon_p$ assume the values of the constant amplitude cases. When the overload is applied, a sudden increase of $\Delta\delta_p$ and $\Delta\varepsilon_p$ takes place, as expected, since the material has not experienced such high loads. After the overload, there is a decrease of $\Delta\delta_p$ and $\Delta\varepsilon_p$, where the

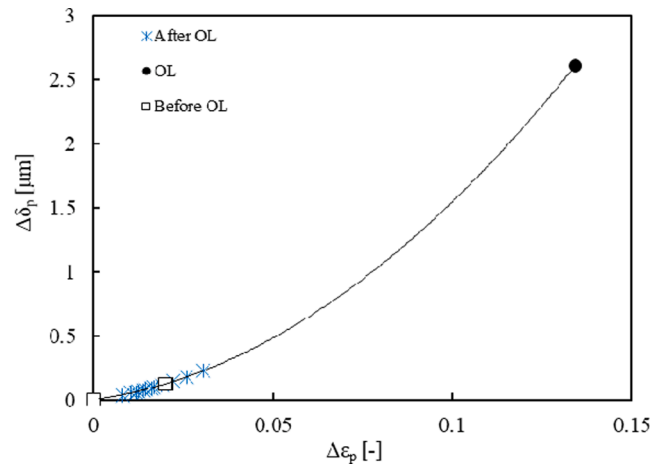


Fig. 13. Effect of a single tensile overload on $\Delta\delta_p$ vs. $\Delta\varepsilon_p$ ($F_{max} = 41.67$ N; $F_{min} = 4.17$ N; $F_{OL} = 60.42$ N; $OLR = 1.50$; $a_{OL} = 16.74$ mm; $\Delta K_{BL} = 10.3$ MPa·m^{0.5}; plane stress).

first crack propagations still show higher values of $\Delta\delta_p$ and $\Delta\varepsilon_p$. This decrease continues until reaching a minimum value. After that, $\Delta\delta_p$ and $\Delta\varepsilon_p$ tend to recover the values observed before the overload. The evolution of these nonlinear parameters with a single tensile overload is similar to the behaviour typically obtained when plotting da/dN in function of the crack growth. There is an increase of da/dN up to a maximum followed by a decrease to a minimum value, after some crack propagation. After the minimum, da/dN consistently tends to the rates exhibited before the overload. Thus, in Fig. 13, as in Fig. 12, a linear relation is observed between $\Delta\delta_p$ and $\Delta\varepsilon_p$ for relatively low values of these parameters, meaning that the link between $\Delta\delta_p$ and $\Delta\varepsilon_p$ is not changed by the application of a single tensile overload. The maximum value, corresponding to the overload cycle, deviates significantly from the linear trend, as was also observed in Fig. 12.

6. Conclusions

FCG in the 2024-T351 aluminium alloy is studied using nonlinear parameters. Experimental tests were performed on 12 mm thick CT specimens in order to obtain FCG rate. The increase of stress ratio from $R = 0.1$ to $R = 0.7$ produced an increase of FCG rate, which indicated the existence of crack closure phenomenon.

A numerical analysis replicated the experimental work in terms of material, geometry and loading conditions but assuming pure plane strain state. The material parameters were fitted using stress-strain loops obtained in cylindrical specimens. The CTOD was measured at the first node behind the crack tip, at a distance of 8 μ m, in order to obtain

the plastic CTOD range, $\Delta\delta_p$. The analysis of the contact status of the first node behind the crack tip was used to predict the crack closure level. For $R = 0.1$ there is no crack closure under plane strain state, while a maximum value $U^*=36\%$ was found for plane stress state. Since experimentally there is an effect of stress ratio, it seems that the crack closure near corner points of the crack front is affecting FCG rate, although the relatively high thickness of the CT specimens (12 mm). The linear regime of CTOD was used to predict effective fatigue threshold in vacuum: $\Delta K_{th,eff} = 3.46 \text{ MPa}\cdot\text{m}^{0.5}$. A ratio of about 2 was found between the numerical prediction of fatigue threshold and the effective value obtained experimentally.

A nearly linear relation was found between da/dN and $\Delta\delta_p$, but a second-order polynomial was proposed for a better fit. The comparison with other aluminium alloys showed that there is a significant influence of material on $da/dN-\Delta\delta_p$ model, which means that for the same crack tip plastic deformation, the FCG rate produced greatly depends on microstructure. The $da/dN-\Delta\delta_p$ was used to predict the effect of stress state and stress ratio. The change from plane stress to plane strain state increased FCG rate once again due to crack closure. Under plane strain state, there is a minor influence of stress ratio in the range $R = 0.1-0.7$, because there is no crack closure. As mentioned, this contradicts the experimental results and indicates the relevance of plane stress behaviour. The extension to negative stress ratios produced significant changes.

Finally, a comparison was made between plastic CTOD and plastic strain at the crack tip. A well-defined relation was found, independent of stress ratio, showing that both parameters can be used to quantify the crack tip deformation. The relation is nearly linear for relatively low values of the parameters. However, some deviation from linearity was observed at high plastic deformation levels, and some influence of stress state was found.

Declaration of Competing Interest

The authors declare that they have no known competing financial interests or personal relationships that could have appeared to influence the work reported in this paper.

Acknowledgement

The authors would like to acknowledge the financial support from Project PTDC/CTM-CTM/29101/2017 – POCI-01-0145-FEDER-029101 funded by FEDER funds through COMPETE2020 - Programa Operacional Competitividade e Internacionalização (POCI) and by national funds (PIDDAC) through FCT/MCTES. This research is also sponsored by FEDER funds through the program COMPETE – Programa Operacional Factores de Competitividade – and by national funds through FCT – Fundação para a Ciência e a Tecnologia –, under the project UIDB/00285/2020, UIDB/00481/2020 and UIDP/00481/2020. Financial support from the Junta de Andalucía through grant reference UMA18-FEDERJA-250 of Programa Operativo FEDER and Subprograma Estatal de Movilidad, del Plan Estatal de I+D+i through grant reference CAS18/00251 is also greatly acknowledged. The authors would also like to acknowledge the funding for open access charge: Universidad de Málaga/CBUA.

References

- Paris PC, Erdogan F. A Critical Analysis of Crack Propagation Laws. *J Basic Eng* 1963;85:528–33.
- Rice JR. The Mechanics of Crack Tip Deformation and Extension by Fatigue. *Fatigue Crack Propagation*, ASTM STP 415. Philadelphia 1967.
- ASTM E647-15, Standard Test Method for Measurement of Fatigue Crack Growth Rates. West Conshohocken, PA: 2015. doi:10.1520/E0647-15E01.2.
- Mokhtarshirzabad M, Lopez-Crespo P, Zanganeh M. Stress intensity factor monitoring under cyclic loading by digital image correlation. *Fatigue Fract Eng Mater Struct* 2018;41:2162–71.
- Elber W. Fatigue crack closure under cyclic tension. *Eng Fract Mech* 1970;2:37–45.
- Vasudevan A, Sadananda K, Louat N. Reconsideration of fatigue crack closure. *Scr Mater* 1992;27:1673–8.
- Lugo M, Daniewicz SR. The influence of T-stress on plasticity induced crack closure under plane strain conditions. *Int J Fatigue* 2011;33:176–85.
- Miarka P, Cruces AS, Seidl S, Malíkova L, Lopez-Crespo P. Evaluation of the SIF and T-stress values of the Brazilian disc with a central notch by hybrid method. *Int J Fatigue* 2020;135:105562.
- Christopher CJ, James MN, Patterson EA, Tee KF. Towards a new model of crack tip stress fields. *Int J Fract* 2007;148:361–71.
- Kujawski D. A new $(\Delta K+K_{max})^{0.5}$ driving force parameter for crack growth in aluminium alloys. *Int J Fatigue* 2001;23:733–40. [https://doi.org/10.1016/S0142-1123\(01\)00023-8](https://doi.org/10.1016/S0142-1123(01)00023-8).
- Norozi AH, Glinka G, Lambert S. A two parameter driving force for fatigue crack growth analysis. *Int J Fatigue* 2005;7:1277–96.
- Pommier S, Lopez-Crespo P, Decreuse PY. A multi-scale approach to condense the cyclic elastic-plastic behaviour of the crack tip region into an extended constitutive model. *Fatigue Fract Eng Mater Struct* 2009;32:899–915.
- Lopez-Crespo P, Moreno B, Sussmel L. Influence of crack tip plasticity on fatigue propagation. *Theor Appl Fract Mech* 2020;108:102667.
- Pommier S, Hamam R. Incremental model for fatigue crack growth based on a displacement partitioning hypothesis of mode I elastic-plastic displacement fields. *Fatigue Fract Eng Mater Struct* 2007;30:582–98.
- Lopez-Crespo P, Pommier S. Numerical analysis of crack tip plasticity and history effects under mixed mode conditions. *Journal of Solid Mechanics and Materials Engineering* 2008;2:1567–76.
- Camas D, Lopez-Crespo P, Gonzalez-Herrera A, Moreno B. Numerical and experimental study of the plastic zone in cracked specimens. *Eng Fract Mech* 2017;185:20–32.
- Vasco-Olmo JM, James MN, Christopher CJ, Patterson EA, Díaz FA. Assessment of crack tip plastic zone size and shape and its influence on crack tip shielding. *Fatigue and Fracture of Engineering Materials and Structures* 2016;39. doi:10.1111/ffe.12436.
- Antunes FV, Rodrigues SM, Branco R, Camas D. A numerical analysis of CTOD in constant amplitude fatigue crack growth. *Theor Appl Fract Mech* 2016;85:45–55.
- Antunes FV, Branco R, Prates PA, Borrego L. Fatigue crack growth modelling based on CTOD for the 7050–T6 alloy. *Fatigue Fract Eng Mater Struct* 2017;40:1309–20.
- Yusof F, Lopez-Crespo P, Withers PJ. Effect of overload on crack closure in thick and thin specimens via digital image correlation. *International Journal of Fatigue* 2013;56. doi:10.1016/j.ijfatigue.2013.07.002.
- Mokhtarshirzabad M, Lopez-Crespo P, Moreno B, Lopez-Moreno A, Zanganeh M. Optical and analytical investigation of overloads in biaxial fatigue cracks. *International Journal of Fatigue* 2017;100 part 2:583–90.
- Vasco-Olmo JM, Díaz FA, Antunes FV, James MN. Characterisation of fatigue crack growth using digital image correlation measurements of plastic CTOD. *Theor Appl Fract Mech* 2019;101:332–41. <https://doi.org/10.1016/j.tafmec.2019.03.009>.
- Vasco-Olmo J, Díaz FA, Antunes FV, James MN. Plastic CTOD as fatigue crack growth characterising parameter in 2024–T3 and 7050–T6 aluminium alloys using DIC. *Fatigue Fract Eng Mater Struct* 2020;1719–30.
- Vasco-Olmo JM, Díaz Garrido FA, Antunes FV, James MN. Plastic CTOD as fatigue crack growth characterising parameter in 2024–T3 and 7050–T6 aluminium alloys using DIC. *Fatigue Fract Eng Mater Struct* 2020;43:1719–30. <https://doi.org/10.1111/ffe.13210>.
- Borges MF, Neto DM, Antunes FV. Numerical simulation of fatigue crack growth based on accumulated plastic strain. *Theor Appl Fract Mech* 2020;108:102676. <https://doi.org/10.1016/j.tafmec.2020.102676>.
- Ferreira FF, Neto DM, Jesus JS, Prates PA, Antunes FV. Numerical Prediction of the Fatigue Crack Growth Rate in SLM Ti-6Al-4V Based on Crack Tip Plastic Strain. *Metals* 2020;10. <https://doi.org/10.3390/met10091133>.
- Chaves V. Ecological criteria for the selection of materials in fatigue. *Fatigue Fract Eng Mater Struct* 2014;37:1034–42.
- Moreno B. Fatigue crack propagation under random loading. 2002.
- Moreno B, Martin A, Lopez-Crespo P, Zapatero J, Dominguez J. Estimations of fatigue life and variability under random loading in aluminum Al-2024T351 using strip yield models from NASGRO. *Int J Fatigue* 2016;91:414–22.
- Chernyatin AS, Lopez-Crespo P, Moreno B, Matvienko YG. Multi-approach study of crack-tip mechanics on aluminium 2024 alloy. *Theor Appl Fract Mech* 2018;98:38–47.
- ASTM E606 / E606M - 12 Standard test method for strain-controlled fatigue testing. 2012.
- Swift HW. Plastic instability under plane stress. *J Mech Phys Solids* 1952;1:1–18. [https://doi.org/10.1016/0022-5096\(52\)90002-1](https://doi.org/10.1016/0022-5096(52)90002-1).
- Lemaitre J, Chaboche J-L. *Mechanics of Solid Materials*. Cambridge University Press; 1990. doi:10.1017/CBO9781139167970.
- Lasdon LS, Waren AD, Jain A, Ratner MW. Design and testing of a generalized reduced gradient code for nonlinear optimization. 1975.
- Menezes LF, Teodosiu C. Three-Dimensional Numerical Simulation of the Deep-Drawing Process using Solid Finite Elements. *J Mater Process Technol* 2000;97:100–6.
- Oliveira MC, Alves JL, Menezes LF. Algorithms and Strategies for Treatment of Large Deformation Frictional Contact in the Numerical Simulation of Deep Drawing Process. *Arch Comput Methods Eng* 2008;15:113–62.
- Borrego LP, Ferreira JM, Costa JM. Fatigue crack growth and crack closure in an AlMgSi alloy. *Fatigue & Fracture of Engineering Materials & Structures* 2001;24:255–65.

- [38] Antunes FV, Prates PA, Camas D, Sarrazin-Baudoux C, Gardin C. Numerical prediction of fatigue threshold of metallic materials in vacuum. *Engineering Fracture Mechanics* 2019;216. doi:10.1016/j.engfractmech.2019.106491.
- [39] Sunder R. Unraveling the Science of Variable Amplitude Fatigue. *J ASTM Int* 2012; 9:1–32.
- [40] Kermanidis AT, Stamatelos DG, Labeas GN, Pantelakis SG. Tensile behaviour of corroded and hydrogen embrittled 2024 T351 aluminum alloy specimen. *Theor Appl Fract Mech* 2006;45:148–58. <https://doi.org/10.1016/j.tafmec.2006.02.004>.
- [41] Avram J. ASTM E647 FCG Testing Standard: Round Robin Fatigue Crack Growth Testing Results. USAF TR 2006-10 2006:18.
- [42] Broek D, Schijve J. The influence of mean stress on the propagation of cracks in aluminium alloy sheet. 1963.
- [43] Pommier S, Risbet M. Time derivative equations for mode I fatigue crack growth in metals. *Int J Fatigue* 2005;27:1297–306. <https://doi.org/10.1016/j.ijfatigue.2005.06.034>.
- [44] Schijve. The significance of fractography for investigations of fatigue crack growth under variable-amplitude loading. *Fatigue & Fracture of Engineering Materials & Structures* 1999;22:87–99. doi:<https://doi.org/10.1046/j.1460-2695.1999.00147.x>.
- [45] Seifi R, Hosseini R. Experimental study of fatigue crack growth in raw and annealed pure copper with considering cyclic plastic effects. *Theor Appl Fract Mech* 2018;94:1–9. <https://doi.org/10.1016/j.tafmec.2017.12.003>.
- [46] Antunes FV, Serrano S, Branco R, Prates P. Fatigue crack growth in the 2050–T8 aluminium alloy. *Int J Fatigue* 2018;115:79–88. <https://doi.org/10.1016/j.ijfatigue.2018.03.020>.
- [47] Patterson EA, Olden EJ. Optical analysis of crack tip stress fields: a comparative study. *Fatigue Fract Eng Mater Struct* 2004;27:623–35.
- [48] da Fonseca JQ, Mummery PM, Withers PJ. Full-field strain mapping by optical correlation of micrographs acquired during deformation. *J Microsc* 2005;218:9–21.
- [49] Sutton MA, Orteu JJ, Schreier H. Image Correlation for Shape, Motion and Deformation Measurements. 2009. <https://doi.org/10.1007/978-0-387-78747-3>.
- [50] Toda H, Sinclair I, Buffière J-Y, Maire E, Khor KH, Gregson P, et al. A 3D measurement procedure for internal local crack driving forces via synchrotron X-ray microtomography. *Acta Mater* 2004;52:1305–17. <https://doi.org/10.1016/j.actamat.2003.11.014>.
- [51] Withers PJ, Lopez-Crespo P, Kyrielleis A, Hung Y-C. Evolution of crack-bridging and crack-tip driving force during the growth of a fatigue crack in a Ti/SiC composite. *Proceedings of the Royal Society A: Mathematical, Physical and Engineering Sciences* 2012;468. doi:10.1098/rspa.2012.0070.
- [52] Withers PJ, Webster PJ. Neutron and Synchrotron X-ray Strain Scanning. *Strain* 2001;37:19–33. <https://doi.org/10.1111/j.1475-1305.2001.tb01216.x>.
- [53] Steuwer A, Rahman M, Shterenlikht A, Fitzpatrick ME, Edwards L, Withers PJ. The evolution of crack-tip stresses during a fatigue overload event. *Acta Mater* 2010;58:4039–52.
- [54] Lopez-Crespo P, Peralta JV, Kelleher JF, Withers PJ. In situ through-thickness analysis of crack tip fields with synchrotron X-ray diffraction. *Int J Fatigue* 2019; 127:500–8.
- [55] Lopez-Crespo P, Camas D, Antunes FV, Yates JR. A study of the evolution of crack tip plasticity along a crack front. *Theor Appl Fract Mech* 2018;98:59–66.
- [56] Garcia-Manrique J, Camas-Peña D, Lopez-Martinez J, Gonzalez-Herrera A. Analysis of the stress intensity factor along the thickness: The concept of pivot node on straight crack fronts. *Fatigue and Fracture of Engineering Materials and Structures* 2018;41. doi:10.1111/ffe.12734.